ORIGINAL ARTICLE

Effect of Remelting on Microstructure Formation for Multi-layer and Multi-track Laser Additive Manufacturing

A. Swain[1] · M. Jegatheesan[1] · P. Rath[1] · S. Mondol[2] ·
A. Bhattacharya[1]

Abstract The effect of remelting during multi-layer and multi-track laser additive manufacturing is presented. A numerical model is developed for simulating layer-by-layer laser melting along longitudinal and transverse planes. The model incorporates the effect of laser movement, heat and species transport, melting, grain nucleation, growth and remelting. The addition of a new layer is modelled using domain translation with a fixed domain size. Formation of parallel tracks is modelled for the transverse plane simulations by implementing the shifting of a variable heat source based on laser position. Simulations are performed for Al–10%Cu with different layer thickness and hatch spacing to study the effect of remelting. Results show that the model can predict melt pool evolution, species segregation, formation and remelting of columnar and equiaxed grains along both transverse and longitudinal planes. The grain density in the remelted region is found to increase with increasing layer thickness.

Keywords Laser additive manufacturing · Multi-layer and multi-track laser melting · Remelting · Species transport · Microstructure formation

1 Introduction

Laser powder bed fusion (LPBF) or selective laser melting (SLM) is a promising laser additive manufacturing process in which the laser passes over a selected portion of the metal or alloy powder bed resulting in melting and subsequent solidification of the region. This is followed by placing another layer of powder with a specified thickness, which subsequently undergoes the laser melting process. Thus, the final product is built in a layer-by-layer manner from the powder raw material.

The final microstructure in this process is governed by the local temperature gradient, cooling rate, species transport, remelting and re-solidification. In recent years, computational models have been developed to study the melt pool evolution and microstructure formation in laser additive manufacturing. Microstructure during laser additive manufacturing has been simulated using cellular automata [1], cellular automata-finite element [2, 3], phase-field [4], Monte Carlo [5, 6] and lattice Boltzmann method [7]. These studies predict the effect of laser parameters and layer thickness on the final microstructure.

The layer-by-layer melting results in remelting of the previously solidified layer during the melting of the subsequent layer. The remelting depends on the process parameters such as laser power, scan speed, layer thickness and lead to change in the microstructure in the remelted zone. Xiong et al. [8] investigated the effect of remelting on tungsten specimens developed using SLM and observed that the remelting process resulted in a finer microstructure. Richter et al. [9] investigated the melt pool dynamics and the influence of remelting on the surface finish of a Co-Cr alloy produced by the SLM method. Boscheto et al. [10] investigated the effect of remelting on the surface roughness of AlSi10Mg alloy parts produced by the LAM method and found that surface quality improved as laser energy density increased. Vaithilingam et al. [11] performed laser melting of Ti6Al4V alloy and found that the decrease in oxide layer was the least in remelted

✉ A. Bhattacharya
   anirban@iitbbs.ac.in

1   School of Mechanical Sciences, IIT Bhubaneswar, Argul, Jatni, Dist. Khurda, Odisha 752050, India

2   Department of Metallurgical and Materials Engineering, NIT Warangal, Hanamkonda, Telangana, India

specimens. Liu et al. [12] investigated remelting during SLM of AlSi10Mg alloy using different scanning strategies to reduce surface irregularity and obtain denser material. Okugawa et al. [13] stated that grain refinement occurs due to heterogeneous nucleation during the remelting for laser additive manufacturing of Al–Si eutectic alloy. Brodie et al. [14] examined the effect of the remelting on Ti25Ta samples produced by SLM and observed that remelting produced denser and more uniform samples.

From experimental studies, it is seen that remelting plays an important role in determining the final grain structure for layer-by-layer laser melting process. In this paper, a numerical model is presented to simulate the melting and microstructure formation during a multi-layer and multi-track laser melting process. The model can predict the melt pool evolution, grain formation and growth, species transport and final microstructure along both the longitudinal plane and transverse plane. In particular, the remelting of previously formed microstructure during the melting of the subsequent layer is studied. Also, the effect of remelting during the formation of multiple parallel tracks is predicted by simulating the evolution of melt pool and microstructure along the plane perpendicular to the laser scanning direction.

2 Mathematical and Numerical Model

The 3D process of laser powder bed fusion is studied using two types of 2D simulations: (a) Along the laser travel direction (longitudinal plane) and (b) along the plane perpendicular to the laser travel direction (transverse plane). For both types of simulations, effect of laser heat source, thermal and species transport, melting, grain nucleation and grain growth are predicted. For the longitudinal plane simulations, the melting of a second layer over the solidified first layer, including the remelting of previous grains, is predicted. The transverse plane simulations are needed to capture the effect of remelting during the formation of a second parallel track partially overlapping the previously formed track.

The overall model is implemented by combining the following sub-models: (a) Laser heat source model, (b) grain nucleation model, (c) heat transfer and melting model, (d) interface dynamics and grain growth model, (e) species transport model and (f) mechanism for formation of multiple layers and multiple tracks.

The interaction of the moving laser with the powder bed is implemented by using a dynamic heat flux boundary condition. For the longitudinal plane simulations, the laser travels across the top surface of the powder bed. This is modelled by using a heat flux term at the top boundary, with intensity variation given by Eq. 1.

$$I = \frac{AP\sqrt{2}}{\sqrt{\pi}r_0}\exp\left[-2\frac{(x - v_l t)^2}{r_o^2}\right] \tag{1}$$

The laser parameters are denoted by the scan speed v_l, laser power P and laser spot radius r_0. For the transverse plane simulations, the laser travels towards the simulation plane and then moves out of the plane. This needs to be incorporated in the simulation by using a double Gaussian variation for the laser intensity. This is done by calculating the peak intensity (I_f) in the simulation plane using Eq. 1. With this intensity at the centre point, the variation in the transverse plane (I_t) is calculated using a Gaussian distribution (Eq. 2).

$$I_t = I_f\exp\left[-2\frac{(x - x_0)^2}{r_o^2}\right] \tag{2}$$

The nucleation of grains within the melt pool depends on the local undercooling, which is calculated from the temperature field T. The rate of nucleation is defined as a function of the undercooling by assigning critical undercooling values at randomly selected nucleation sites [15]. For nucleation along the edges of the melt pool, separate random distribution of nuclei is defined. In the present model, the effect of dendrite fragmentation due to convection, and its effect on increase in nucleation sites have not been considered.

A grain number parameter is defined to identify each grain uniquely. During the simulation, a nucleus is activated if the local undercooling at that point becomes higher than the critical undercooling for the corresponding nucleus. When a nucleus is activated, it is assigned a unique grain number and a random orientation angle (θ_r). Thus, the solid region corresponding to each dendrite can be identified and differentiated based on the grain number.

The heat transfer in the domain is calculated by solving the volume averaged energy conservation equation (Eq. 3) formulated in terms of enthalpy $h = c_p T + f_l L$. The enthalpy is a function of the sensible energy ($c_p T$), liquid fraction f_l and latent heat of fusion L. Cooling is imposed on the domain using the source term S_{cr} [16].

$$\frac{\partial(\rho h)}{\partial t} = \nabla \cdot (k\nabla T) - S_{cr} \tag{3}$$

The phase change is modelled using a sharp interface method. The liquid fraction is calculated from h, using the interface temperature T_i. The interface temperature depends on the interfacial energy and the local species concentration, as given in Eq. 4.

$$T_i = T_m - \frac{T_m\gamma(\theta, \theta_r)\kappa}{L} - m(C_0 - V) \tag{4}$$

For calculating the value of T_i, the curvature κ is calculated using f_l, and the concentration C is obtained from the species conservation equation (Eq. 5). The effect of preferred growth directions and the grain orientation are incorporated by using anisotropic surface tension $\gamma(\theta, \theta_r)$ and random orientation angle θ_r [16].

$$\frac{\partial(\rho C)}{\partial t} = \nabla \cdot (\rho D \nabla V) \tag{5}$$

The species conservation equation governs the species transport, which depends on partitioning at the interface and diffusion in the melt pool. This is formulated following the concentration potential (V) method proposed by Voller [17]. More details about the heat transfer and solidification model are given in [16]. The treatment of simultaneous melting at the front and solidification at the rear portion of the melt pool is given in [18]. The governing equations and sub-models remain same for both longitudinal and transverse plane simulations, except the implementation of the laser heat source.

The layering mechanism is modelled by using a domain translation scheme. After the completion of each layer, all the parameter values are shifted downward by a distance equal to the specified layer thickness. The top part of the domain is again defined as a new powder bed, and the process of laser melting is repeated. This represents the movement of the simulation domain after formation of each layer so that the top layer is at the top boundary of the domain. More detail about the layering mechanism is presented in [19]. The powder bed for each layer is implemented by defining the material properties as function of the powder bed porosity φ.

The formation of multiple parallel tracks can be simulated in the transverse plane. For this, after the completion of each track, the laser beam is shifted laterally by a distance equal to the hatch spacing. Subsequently, the process of melting is repeated based on the variation of laser intensity as discussed previously.

The effect of change of volume during the melting of the powder bed and during subsequent solidification is not considered in the present model. It is assumed that the air in the powder bed gets trapped in the liquid during melting and solidification due to the rapid cooling process. Thus, the volume of the alloy and the porosity are considered to remain unchanged during the process.

The model is implemented using an explicit finite volume method, and the implemented algorithm is executed using the Fortran 90 language.

3 Results and Discussion

The model has been validated for heat transfer, species transport, dendrite growth and microstructure formation

previously [16]. Validation of the melting model is given in [19]. For the present study, the longitudinal plane simulations are performed with a rectangular domain of $3 \text{ mm} \times 1 \text{ mm}$, as shown in Fig. 1. Formation of two layers during left-to-right laser travel is studied with Al—10% Cu as the alloy composition. For all the simulations, the laser parameters are specified as 1000 W power, 1 m/s scan speed, 0.1 mm spot radius and laser absorptivity equal to 0.7. The properties of Al–Cu alloy [20] and the simulation parameters are presented in Table 1.

Figures 1 and 2 show the melt pool shape, Cu concentration and microstructure in the longitudinal plane and transverse plane, respectively. Figures 1a and 2a show the liquid fraction contours during the melting process. The shape of the melt pool can be observed from these two figures. Figures 1b and 2b present the Cu concentration contours and thus show the segregation pattern in the solidified regions. Figures 1c and 2c show the grain number contours, which are used to represent the grain structure.

It is seen that the melt pool has an asymmetrical shape due to the laser movement towards the right side of the domain. Melting occurs at the front edge of the pool, while grains nucleate and grow at the rear portion. The concentration contours show horizontal segregation. The remelting of the previous layer also influences the species transport in the melt pool. The microstructure plot shows formation of columnar grains, which are inclined towards the right demonstrating that the model captures the effect of scan direction on the grain structure.

Figure 2 shows the results for the formation of two parallel tracks in the transverse plane. For the transverse plane simulations, a domain of $2 \text{ mm} \times 1 \text{ mm}$ is considered with a hatch spacing (centre-to-centre distance) of 0.2 mm. Formation of circular melt pool is seen with columnar grains along the edges of the melt pool and equiaxed grains in the interior portion. The variation of concentration results from the solute partitioning during grain growth.

To study the effect of remelting, simulations are performed with different layer thicknesses varying from 0.08 to 0.24 mm in steps of 0.04 mm. As the other parameters are fixed, this results in different degree of remelting in each case. Figure 3 shows the concentration contours and microstructure for layer thickness of 0.24 mm and 0.08 mm. For the larger layer thickness, there is less remelting and thus similar concentration patterns are seen for each layer. The second layer shows the nucleation and growth of larger grains as compared to the first layer. In contrast, for the smaller layer thickness, there is considerable remelting. The grains in the first layer get remelted and subsequently grow during the solidification of the second layer, resulting in continuous columnar grains in the two layers.

The variation of concentration and grain density in the remelted region are compared by plotting the scaled standard

Fig. 1 Longitudinal plane
simulation results at $t = 8.4$ ms:
a melt pool shape, **b** Cu
concentration contours, and **c**
microstructure
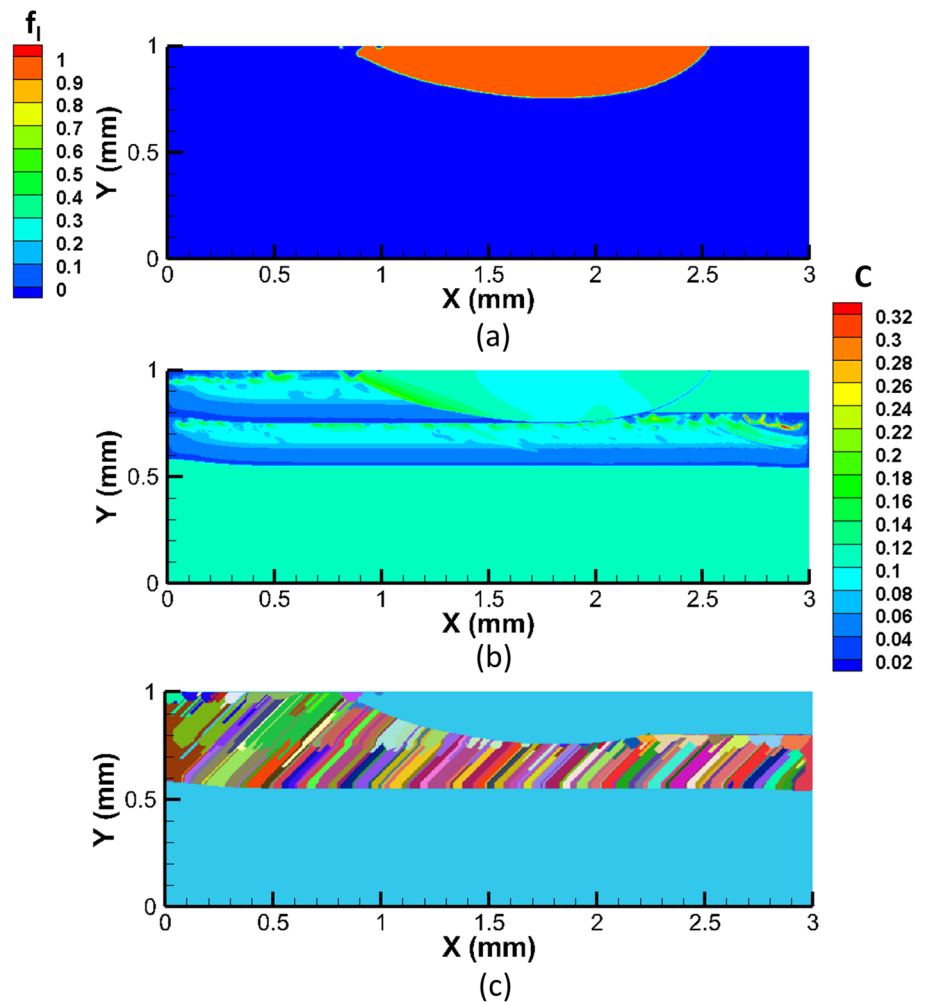
deviation (SSD) of concentration and grain density for different values of layer thickness (Fig. 4). It is seen that the SSD decreases with increasing layer thickness denoting higher uniformity in the remelted region. The grain density increases with increase of layer thickness, representing the formation of new grains. With increase in layer thickness there is less remelting of previous grains. As a result, the growth of previous grains is reduced, and new equiaxed grains are generated leading to increase of grain density.

To see the effect of different overlaps during the formation of parallel tracks, simulations are performed with hatch spacing varying from 0.1 mm to 0.4 mm in steps of 0.1 mm. The concentration contours and microstructure for hatch spacing of 0.1 mm and 0.4 mm are compared in Fig. 5, while Fig. 6 shows the variation of SSD and grain density for different hatch spacing. For smaller values of hatch spacing, most of the initially formed microstructure gets remelted

and columnar grains are formed. For larger hatch spacing, the extent of remelting gets reduced considerably. Each track shows similar microstructure with columnar grains along the edges and equiaxed grains at the centre. During the formation of the second track, the previous grains get partially remelted and start growing when there is solidification in the second melt pool. This results in columnar grains growing from the periphery of the melt pool towards the interior region. Subsequently, some portion of the melt pool reaches the threshold undercooling values for nucleation, which results in the formation of equiaxed dendrites with random orientation. The transition from columnar to equiaxed dendrites depends on the nucleation parameters such as maximum nucleation density and critical undercooling.

The concentration variation depends on the partitioning of solute during grain growth. The SSD values show that the concentration variation is much higher in this plane as

Table 1 Thermophysical properties (Al–Cu alloy) [20] and simulation parameters

Parameter	Symbol	Value
Density of the solid and liquid phase (kg/m^3) (taken)	ρ_s, ρ_l	2580.0
Dynamic viscosity (Ns/m^2)	M	0.0013
Thermal conductivity of liquid phase (W/mK)	k_l	80
Thermal conductivity of solid phase (W/mK)	k_s	180
Specific heat of the liquid phase (J/kgK)	C_{pl}	1130.0
Specific heat of the solid phase (J/kgK)	C_{ps}	1030.0
Latent heat of fusion (J/kg)	L	3.77×10^5
Mass diffusivity of the liquid phase (m^2/s)	D_l	5.0×10^{-9}
Partition coefficient	k_p	0.173
Slope of the liquidus line (K/% C)	M	-3.42
Thermal coefficient of volumetric expansion (1/K)	β_T	2.0×10^{-5}
Solutal coefficient of volumetric expansion	β_C	0.025
Surface tension coefficient (N/mK)	Σ	0.72×10^{-4}
Laser power (W)	P	1000
Laser scan speed (m/s)	v_l	1.0
Laser spot radius (mm)	r_0	0.1
Absorptivity of laser	A	0.7
Porosity of powder bed	$\in$	0.2
Layer thickness (mm)	l_t	0.08. 0.12, 0.16, 0.2, 0.24
Hatch thickness (mm)	h_t	0.1, 0.2, 0.3, 0.4
Mean undercooling for nucleation (K)	ΔT_m	0.1
Standard deviation of undercooling for nucleation (K)	ΔT_σ	0.01
Nucleation density (mm^{-2})	n	4000

compared to the longitudinal plane. There is not much variation in both SSD and grain density with respect to change in hatch spacing. For the simulations presented, the laser parameters such as laser power, scan speed and laser spot radius have been kept constant for all the cases. Thus, the main change in the grain structure and segregation pattern occurs due to the extent of overlap and remelting between the adjacent layers and tracks. The time gap between the formation of each track results in similar cooling characteristics for all the cases, independent of the extent of overlap.

Predictions by the present model are similar to the experimental results for melt pool shape and grain structure given in [21–23]. For example, the simulation results show similar pattern of the melted region and grain structure as given in Wang et al. [21] for both transverse plane and longitudinal plane. Similar to [21], the region near the melt pool interface contains a band of columnar grains and the interior region contains equiaxed grains. The predictions from our multi-track simulations (Fig. 5) are similar to the experimental

results for grain structure for multiple layers and tracks given in [22, 23].

4 Conclusion

Simulation results along the longitudinal and transverse planes show that the model is capable of predicting the formation of melt pool, nucleation and growth of columnar and equiaxed dendrites, remelting of grains and species transport during a multi-layer and multi-track laser melting process. It is found that the grain density along the longitudinal plane increases from less than 300 to about 2500 grains/mm^2 with increase in layer thickness from 0.08 mm to 0.24 mm. Thus, lower remelting results in higher grain density in this case. Transverse plane simulations show less variation, with the grain density decreasing from about 3150 to 2800 and then increasing to 3400 grains/mm^2. The model can be used in future to perform a more exhaustive study considering laser powder bed melting with large number of layers and tracks.

Fig. 2 Transverse plane simulation results at $t = 2.67$ ms: **a** melt pool shape, **b** Cu concentration contours and **c** microstructure
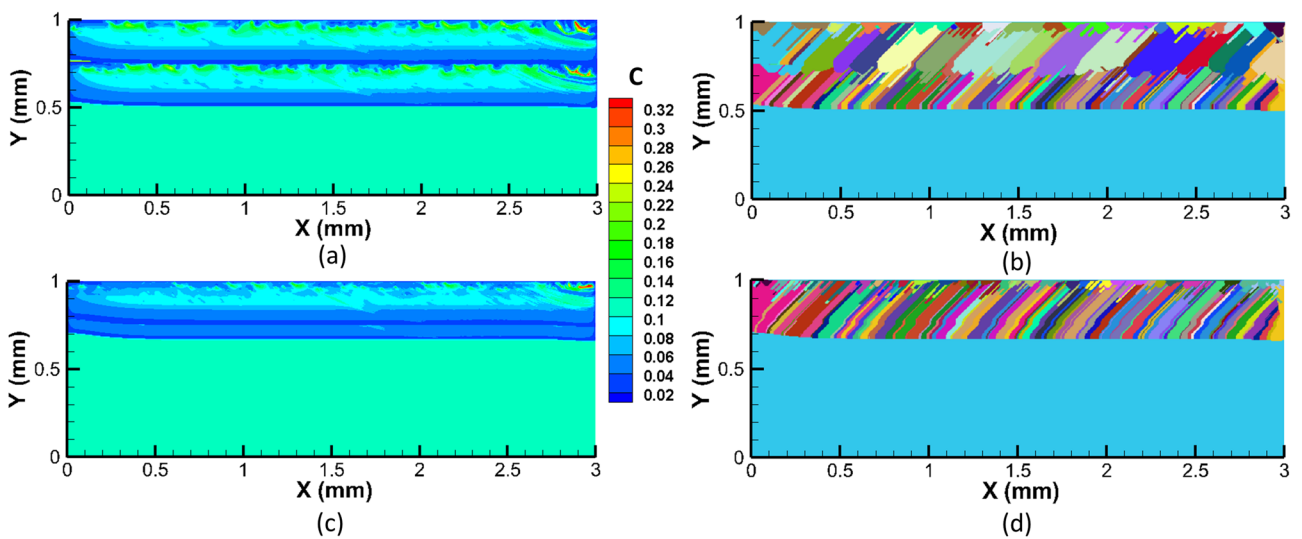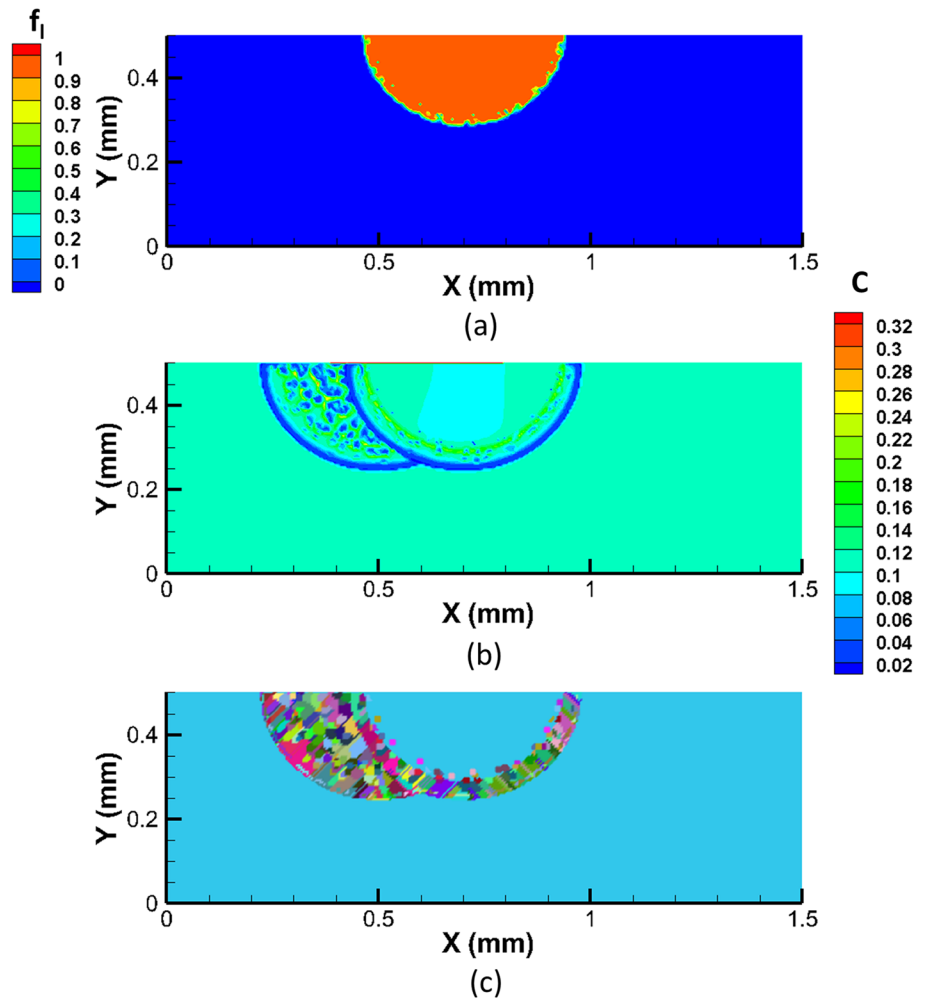

(a)

(b)

(c)

Fig. 3 Concentration contours and microstructure for layer thickness of 0.24 mm (**a, b**) and 0.08 mm (**c, d**) after complete solidification ($t = 12$ ms)
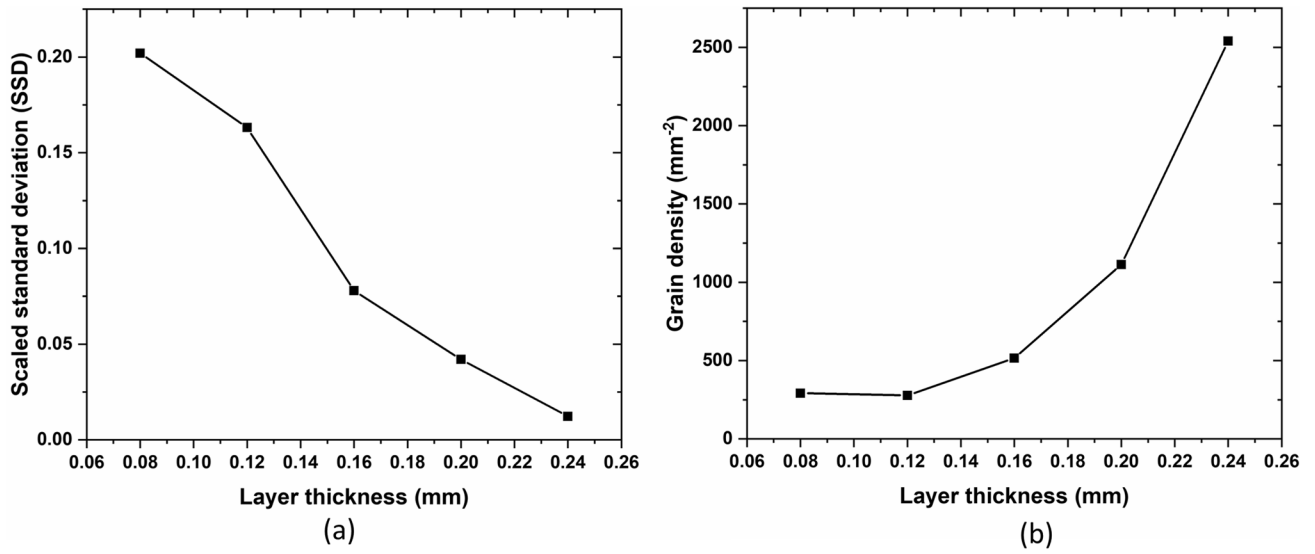
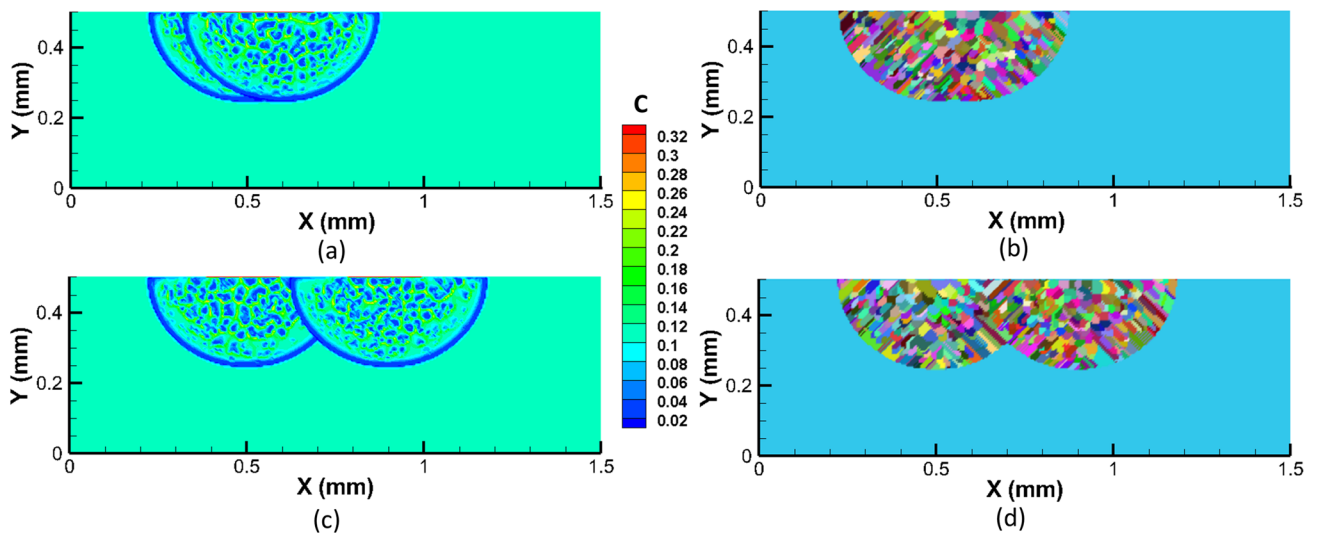**Fig. 4** Effect of layer thickness on **a** SSD and **b** grain density in the remelted region

Fig. 5 Concentration contours and microstructure for hatch spacing of 0.1 mm (**a**, **b**) and 0.4 mm (**c**, **d**) after complete solidification ($t = 4.25$ ms)
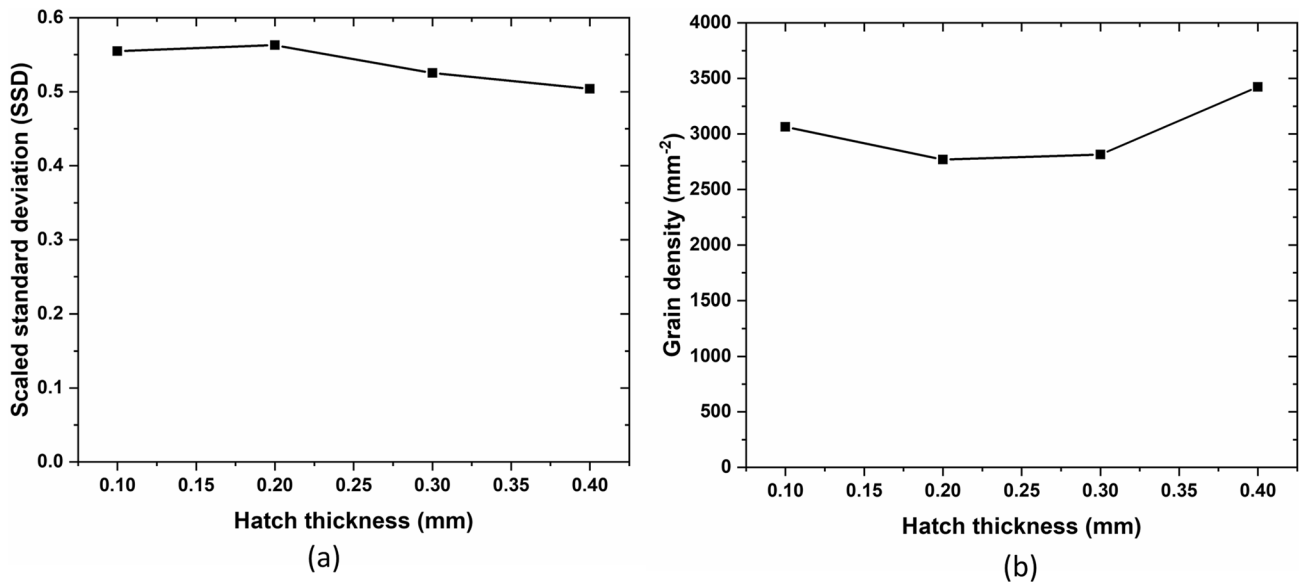
Fig. 6 Effect of hatch spacing on **a** SSD and **b** grain density in the remelted region

References

1. Zinoviev A, Zinovieva O, Ploshikhin V, Romanova V, and Balokhonov R, *Mater Design* **106** (2016) 321. https://doi.org/10.1016/j.matdes.2016.05.125
2. Zhang J, Liou F, Seufzer W, and Taminger K, *Addit Manuf* **11** (2016) 32. https://doi.org/10.1016/j.addma.2016.04.004
3. Yin H, and Felicelli S D, *Acta Materialia* **58** (4), (2010) 1455. https://doi.org/10.1016/j.actamat.2009.10.053
4. Sahoo S, and Chou K, *Addit Manuf* **9** (2016) 14. https://doi.org/10.1016/j.addma.2015.12.005
5. Rodgers T M, Madison J D, and Tikare V, *Comput Mater Sci* **135** (2017) 78. https://doi.org/10.1016/j.commatsci.2017.03.053
6. Pauza J G, Tayon W A, and Rollett A D, *Model Simul Mater Sci Eng* **29** (5), (2021) 055019. https://doi.org/10.1088/1361-651X/ac03a6
7. Rai A, Markl M, and Körner C, *Comput Mater Sci* **124** (2016) 37. https://doi.org/10.1016/j.commatsci.2016.07.005
8. Xiong Z, Zhang P, Tan C, Dong D, Ma W, and Yu K, *Adv Eng Mater* **22** (3), (2020) 1901352. https://doi.org/10.1002/adem.201901352
9. Richter B, Blanke N, Werner C, Parab N D, Sun T, Vollertsen F, and Pfefferkorn F E, *CIRP Ann* **68** (1), (2019) 229. https://doi.org/10.1016/j.cirp.2019.04.110
10. Boschetto A, Bottini L, and Pilone D, *Int J Adv Manuf Technol* **113** (2021) 2739. https://doi.org/10.1007/s00170-021-06775-3
11. Vaithilingam J, Goodridge R D, Hague R J, Christie S D, and Edmondson S, *J Mater Process Technol* **232** (2016) 1. https://doi.org/10.1016/j.jmatprotec.2016.01.022
12. Liu B, Li B Q, and Li Z, *Results Phys* **12** (2019) 982. https://doi.org/10.1016/j.rinp.2018.12.018
13. Okugawa M, Ohigashi Y, Furishiro Y, Koizumi Y, and Nakano T, *J Alloys Compd* **919** (2022) 165812. https://doi.org/10.1016/j.jallcom.2022.165812
14. Brodie E G, Medvedev A E, Frith J E, Dargusch M S, Fraser H L, and Molotnikov A, *J Alloys Compd* **820** (2020) 153082. https://doi.org/10.1016/j.jallcom.2019.153082
15. Rappaz M, and Gandin C A, *Acta Metallurgica et Materialia* **41** (2), (1993) 345. https://doi.org/10.1016/0956-7151(93)90065-Z
16. Jegatheesan M, and Bhattacharya A, *Comput Mater Sci* **186** (2021) 110072. https://doi.org/10.1016/j.commatsci.2020.110072
17. Voller V R, *Int J Heat Mass Transf* **51** (3–4), (2008) 823. https://doi.org/10.1016/j.ijheatmasstransfer.2007.04.025
18. Swain A, Jegatheesan M, Jakhar A, Rath P, and Bhattacharya A, *J Mater Eng Perf* (2023). https://doi.org/10.1007/s11665-023-08519-8
19. Swain A, Khan P M, Rath P, and Bhattacharya A, *J Laser Appl* **33** (4), (2021) 042040. https://doi.org/10.2351/7.0000541
20. Založnik M, and Šarler B, *Mater Sci Eng: A* **413** (2005) 85. https://doi.org/10.1016/j.msea.2005.09.056
21. Wang T, Zhu Y Y, Zhang S Q, Tang H B, and Wang H M, *J Alloys Compd* **632** (2015) 505. https://doi.org/10.1016/j.jallcom.2015.01.256
22. Elmer J W, Ellsworth G F, Florando J N, Golosker I V, and Mulay R P, *Metall Mater Trans A* **48** (2017) 1771. https://doi.org/10.1007/s11661-017-3996-y
23. Deb Roy T, Wei H L, Zuback J S, Mukherjee T, Elmer J W, Milewski J O, Beese A M, Wilson-Heid A D, De A, and Zhang W, *Prog Mater Sci* **92** (2018) 112. https://doi.org/10.1016/j.pmatsci.2017.10.001